

SYNTHETIC JET FORCING OF LARGE-SCALE FLUCTUATIONS IN A TURBULENT BOUNDARY LAYER

Randy K. R. Belanger

Institute for Aerospace Studies
University of Toronto
Toronto, Ontario, M3H 5T6 Canada
randy.belanger@utoronto.ca

David W. Zingg

Institute for Aerospace Studies
University of Toronto
Toronto, Ontario, M3H 5T6 Canada
dwz@utias.utoronto.ca

Philippe Lavoie

Institute for Aerospace Studies
University of Toronto
Toronto, Ontario, M3H 5T6 Canada
lavoie@utias.utoronto.ca

ABSTRACT

Having both a footprint in the near-wall region, and a modulating effect on the energetic small-scale fluctuations in the near-wall region, large scale fluctuations in the log layer play an important role in a turbulent boundary layer. Our objective is to target the large-scale structures with the intention of indirectly influencing the small-scale structures near the wall. By forcing the large-scales, and, more generally, the turbulent boundary layer, we hope to understand how we can manipulate the turbulence. In this work we use spanwise-oriented rectangular synthetic jets to provide the forcing and are able to show that we can reduce the amplitude of the large wavelength fluctuations from the wall up to the height of the synthetic jet penetration. Furthermore, we show that the correlation of the velocity fluctuations in the boundary layer with the wall shear stress fluctuations is reduced for the large wavelengths in the log-region of the boundary layer.

INTRODUCTION

The friction Reynolds number—defined as $Re_\tau = \delta u_\tau / \nu$, where δ is the boundary layer thickness, u_τ is the friction velocity, and ν is the kinematic viscosity—is typically used to characterize turbulent boundary layer flow. At low Re_τ , the turbulent boundary layer is dominated by small scales close to the wall where there is believed to be a cycle that governs the turbulence generation. This process is reported to involve the quasi-streamwise legs of hairpin vortices which generate high- and low-speed streamwise velocity streaks through advection, and which subsequently generate new hairpin vortices through an instability (Walleffe, 1997; Jiménez & Pinelli, 1999; Schoppa & Hussain, 2002). In addition to this near-wall process involving small scales, which follow inner scaling, the larger scales in the log-region, which follow outer scaling, also have an influence. First, the energy near the wall includes a contribution from large wavelengths. These large scale structures are coherent with the energetic large scale structures in the log-region, and so are said to be the ‘footprint’ of the large scale

log-region structures on the near-wall region (del Álamo & Jiménez, 2003; Hutchins & Marusic, 2007a). As Re_τ is increased, the energy associated with the large scales in the near-wall region increases, while the energy of the small-scale motions at the same wall-normal location remains essentially constant (Hoyas & Jiménez, 2006; Marusic *et al.*, 2010). Furthermore, an increasingly larger proportion of the turbulence kinetic energy is concentrated in the log-region of the boundary layer and at larger scales (Hutchins & Marusic, 2007a; Marusic *et al.*, 2010). This is important since, for applications of engineering interest, the Re_τ is typically much higher than can be measured in lab-based wind tunnels.

Additionally, there is also a modulating effect of these large scales on the small scales in the near-wall region, as noted by Hutchins & Marusic (2007b) and Mathis *et al.* (2009). In the near-wall region both a frequency and an amplitude modulation effect is seen whereby the presence of large-scale low-speed streaks results in lower amplitude, lower frequency small-scale motions, with the reverse being true for large-scale high-speed streaks (Ganapathisubramani *et al.*, 2012). Thus, the large scales do not just add a large wavelength contribution to the near-wall energy, but also actively influence the energetic near-wall small scales. It is thus clear that the large scale fluctuations, which are most active in the log region of the boundary layer, play an important role in the near-wall turbulence.

In what will be shown below, we use synthetic jet actuators with rectangular orifices whose spanwise dimension is matched to the reported spanwise extent of large-scale structures in the log-region. Synthetic jet actuators consist of a vibrating diaphragm, cavity, and orifice. The oscillatory motion of the diaphragm causes alternating blowing and suction of the working fluid, the turbulent boundary layer in this case, through the orifice. Since they can generate momentum without net mass flux, synthetic jet actuators are also referred to as zero net mass flux actuators.

The emergent structure of a synthetic jet formed in a crossflow is highly dependent on its frequency, f , and amplitude (jet velocity, \bar{u}_j). These can be nondimensionalized

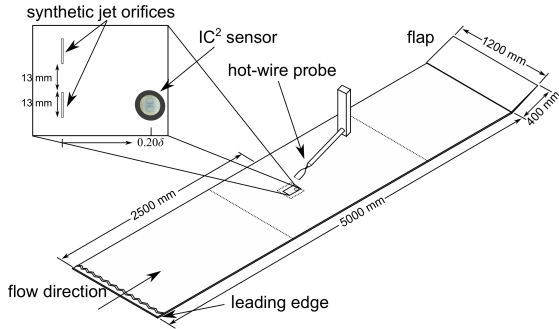


Figure 1. Schematic of the experimental setup. Insert shows an enlarged view of the region near the synthetic jet actuator.

in outer units, giving the Strouhal number, St , and the blowing ratio, r . These parameters can also be combined to form a nondimensional stroke length L/δ , which describes the length of the column of fluid over the expulsion stroke:

$$St = \frac{f\delta}{u_\infty}, \quad r = \frac{\bar{u}_j}{u_\infty}, \quad \frac{L}{\delta} = \frac{r}{St} \quad (1)$$

The jet velocity, here, is the phase-averaged expulsion velocity averaged over the entire jet cycle:

$$\bar{u}_j = \frac{1}{2\pi} \int_0^\pi \tilde{u}_j(\phi) d\phi \quad (2)$$

where $\tilde{u}_j(\phi)$ is the phase-averaged jet velocity, and ϕ is the phase. This equation assumes that the blowing half of the cycle is from $0 < \phi < \pi$.

The vortical structures of pulsed jets and synthetic jets for different r and St issuing from circular orifices into a laminar boundary layer have been studied by Sau & Mahesh (2008) and Jabbar & Zhong (2008), respectively. For example, Sau & Mahesh (2008) found that for low r , and irrespective of L/δ the resultant vortical structure is a hair-pin vortex. At higher r , the jet is able to penetrate further into the boundary layer and takes on two different structures; at low L/δ it forms an isolated vortex ring inclined in the crossflow, and at higher L/δ it forms a declined vortex ring with a trailing jet column. It is expected that these different vortical structures will have distinct effects on a turbulent boundary layer. In addition, rectangular orifices add extra complexity as the rollup of the sheet of vorticity from the jet results in two vortex pairs whose relative strength depends on the aspect ratio of the orifice, as noted by Van Buren *et al.* (2014).

EXPERIMENTAL SETUP

A schematic of the experimental setup is shown in Figure 1. All experiments were conducted in the closed loop wind tunnel in the Flow Control and Experimental Turbulence lab at the University of Toronto Institute for Aerospace Studies. The test section of this wind tunnel consists of two removable sections, each 2.5 m in length with a cross-section measuring 0.8 m \times 1.2 m (height \times width). Three aluminum plates, each spanning the width of the test section and together spanning the length of the test section,

Table 1. Selected nominal properties of the unforced zero pressure gradient turbulent boundary layer flow at the measurement location.

δ	δ^*	θ	u_∞	u_τ
43 mm	7.2 mm	5.2 mm	9.4 m/s	0.37 m/s

were installed high enough (between 1/3 and 1/4 of the test section height) to prevent effects from the boundary layer that develops on the wind tunnel floor. An asymmetrical leading edge, designed by Hanson *et al.* (2012), is included to reduce the adverse pressure gradient at the leading edge. Just downstream of the leading edge is a double-layer of zig-zag tape which is used to trip the flow to turbulence. Furthermore, a hinged flap is located at the trailing edge to control the location of the stagnation line. A zero pressure gradient was established by adjusting the corner fillets on the test sections, and the angle of attack of the plate. The properties of the baseline turbulent boundary layer at the measurement location are given in Table 1. Along with $\nu = 1.58 \times 10^{-5} \text{ m}^2/\text{s}$, the combination of the parameters in this table result in $H = 1.38$, $Re_\theta = 3100$, and $Re_\tau = 1000$.

Located just downstream of the midpoint of the test section, and centered midspan, is a removable synthetic jet actuator plate mounted flush with the boundary layer plate. The synthetic jet actuator consists of a vibrating diaphragm, in the form of a Visaton SC 8N loudspeaker, oscillating against a disk-shaped cavity, which alternately ingests and expels fluid through a rectangular-shaped orifice. The spanwise dimension of the orifice is chosen to match the spanwise dimension of the large-scale streaky structures in the log-region of the turbulent boundary layer in Table 1. These are documented to be about $0.25\text{--}0.45\delta$, where δ is the boundary layer thickness (Ganapathisubramani *et al.*, 2005). The streamwise dimension of the jet orifice is 1 mm, and the spanwise dimension is 13 mm, which corresponds to roughly 0.3δ for the turbulent boundary layer described in Table 1. The sinusoidal input voltage was created using a Rigol DG1022 function generator and subsequently amplified by a Crown XTi 1002 audio amplifier before being sent to the loudspeaker.

Measurements of streamwise velocity fluctuations were made with a hot-wire attached to a wall-normal Velmex X-slide traverse suspended vertically from the ceiling of the test section. The hot-wire itself was fabricated from 2.5 μm tungsten wire. This wire was coated with copper except for a small active region having $l^+ \approx 14$ and $l/d \approx 225$. The hot-wire was operated with a Dantec StreamLine constant temperature anemometer at an overheat ratio of 1.8.

The measurements of wall shear stress were made with the IC² CS-D100 capacitive shear stress sensor and associated sensor control unit described in Mills *et al.* (2018). For all of the measurements discussed below, the hot-wire was positioned directly above the shear stress sensor and allowed to traverse throughout the boundary layer to measure correlations between streamwise velocity fluctuations and wall-shear stress fluctuations. Both of these sensors were situated at a distance of approximately 2δ downstream of the centerline of the orifice. All measurements were sampled at a rate of 25 kHz and low-pass filtered at about 10 kHz.

RESULTS

The following results show a number of plots which make use of the power spectral density. The general one-sided cross power spectral density (CPSD), ϕ_{uv} , for fluctuating quantities u and v is defined as:

$$\phi_{uv}(y, f) = 2 \frac{\mathcal{F}[u(y, t)] \mathcal{F}^*[v(y, t)]}{f_s} \quad (3)$$

where $\mathcal{F}[u(y, t)]$ is the Fourier transform of a discrete time series $u(y, t)$ at wall-normal position y , and f_s is the sampling frequency of both u and v . The CPSD is complex unless $u = v$, in which case all values are real (and the resulting spectrum is the auto power spectral density or simply the power spectral density). Furthermore, the CPSD has the following property:

$$\int_0^\infty \text{Real}\{\phi_{uv}(y, f)\} df = \overline{u(y, t)v(y, t)} \quad (4)$$

where barred quantities represent a time-average. To ensure that equal area under the curve contributes equally to the RMS quantities when viewed on a logarithmic frequency scale, the CPSD is premultiplied by the frequency since:

$$\int_0^\infty f \text{Real}\{\phi_{uv}(y, f)\} d[\ln(f)] = \overline{u(y, t)v(y, t)} \quad (5)$$

Finally, by applying Taylor's hypothesis, we can convert the frequency, f , to streamwise wavelength, λ_x , through $\lambda_x = u_c/f$, where u_c is the convection velocity. We use $u_c = \bar{u}(y)$. We can thus rewrite Equation 5 as:

$$\int_0^\infty k_x \text{Real}\{\phi_{uv}(y, k_x)\} d[\ln(k_x)] = \overline{u(y, t)v(y, t)} \quad (6)$$

where $k_x = 2\pi/\lambda_x$ is the streamwise wavenumber, and $\phi_{uv}(y, k_x) = \phi_{uv}(y, f)\bar{u}(y)/2\pi$ is the CPSD converted to the streamwise wavenumber domain from the frequency domain using Taylor's hypothesis.

Some of the results are shown as a difference in the CPSD with and without synthetic jet forcing: $\Delta\phi_{uv} = \phi_{uv, \text{controlled}} - \phi_{uv, \text{uncontrolled}}$.

Heat Transfer Effect

When the hot-wire is positioned very close to the wall, and hence the wall shear stress sensor, there can be significant heat transfer from the hot-wire to the wall shear stress sensor. This heat transfer seems to cause the wall shear stress sensor to fluctuate more strongly, as can be seen in the pre-multiplied power spectral density (PSD) of wall shear stress fluctuations, $f\phi_{\tau_w\tau_w}$, as a function of hot-wire wall-normal distance in Figure 2. When the hot-wire is close to the wall there is a positive shift in the power spectral density for all frequencies. Two vertical lines are included to indicate boundaries of regions where there is a difference in the τ_w' PSD. When the hot-wire is at wall-normal locations below the solid black line, there is a strong impact of the hot-wire on the τ_w' PSD. Measurements made of τ_w' in this location are not trustworthy. Between the solid black line and the dashed black line, there is only a mild effect from the hot-wire heat transfer. Care must be taken when

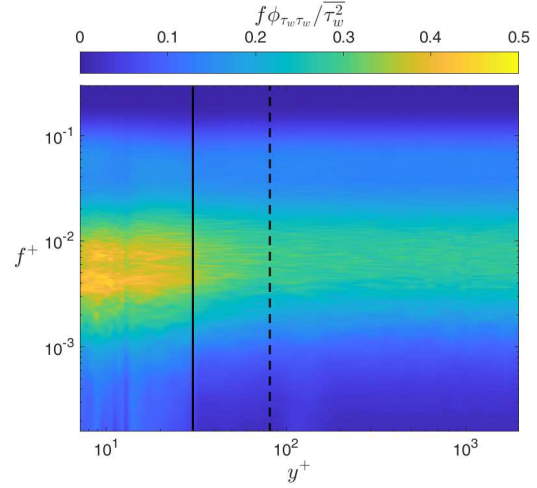


Figure 2. Pre-multiplied power spectral density of wall shear stress fluctuations as a function of wall-normal distance.

interpreting the results when the hot-wire is at these wall-normal locations. Above the dashed black line there does not appear to be any effect of the hot-wire on the wall-shear stress signal. These two vertical lines will be included on all subsequent plots involving simultaneous measurements of u' and τ_w' .

Effect of synthetic jet forcing

A total of four synthetic jet cases will be explored. This includes three cases used to compare the effect of the forcing at different r ; $r = \{0.45, 0.88, 1.3\}$ at $St = 2.3$. One further case is used to compare the effect of St , namely $St = 0.045$, $r = 0.5$, on the turbulent boundary layer¹.

We look first at the effect of synthetic jet forcing on the fluctuating streamwise velocity, u' , across both streamwise wavelength and throughout the height of the boundary layer. For each synthetic jet case, the power spectral density (PSD) is measured with the jet both on and off at all locations in the boundary layer, and the difference computed. Figure 3 shows the comparison across r , and Figure 4 is used in conjunction with Figure 3a to compare across St .

Looking first at the effect as a function of r in Figure 3, we see that for all cases there is a decrease in the contribution to u' from the largest wavelength scales in the flow. This effect stretches from the wall into at least the log-region for the cases tested. At higher y there is a broadband increase in u' that occurs for all scales in the flow, with the strongest increase occurring close to the wavelength associated with the frequency of the synthetic jets, shown as the solid black line. The y location where this broadband increase in u' occurs is believed to be the height at which the spanwise vortex from the synthetic jet crosses our measurement plane at $x = 2\delta$ downstream of the orifice centerline, since it increases with increasing r as expected, and is associated with a decrease in $\bar{u}(y)$ (not shown). It is unclear whether the increase in broadband u' is the result of a turbulent jet, or the breakdown of larger scale structures into smaller ones. The larger changes seen in the higher r cases are believed to be the result of higher shear associated with a faster jet issuing into a boundary layer. Finally, at higher

¹The difference between $r = 0.45$ and $r = 0.5$ is expected to be minimal

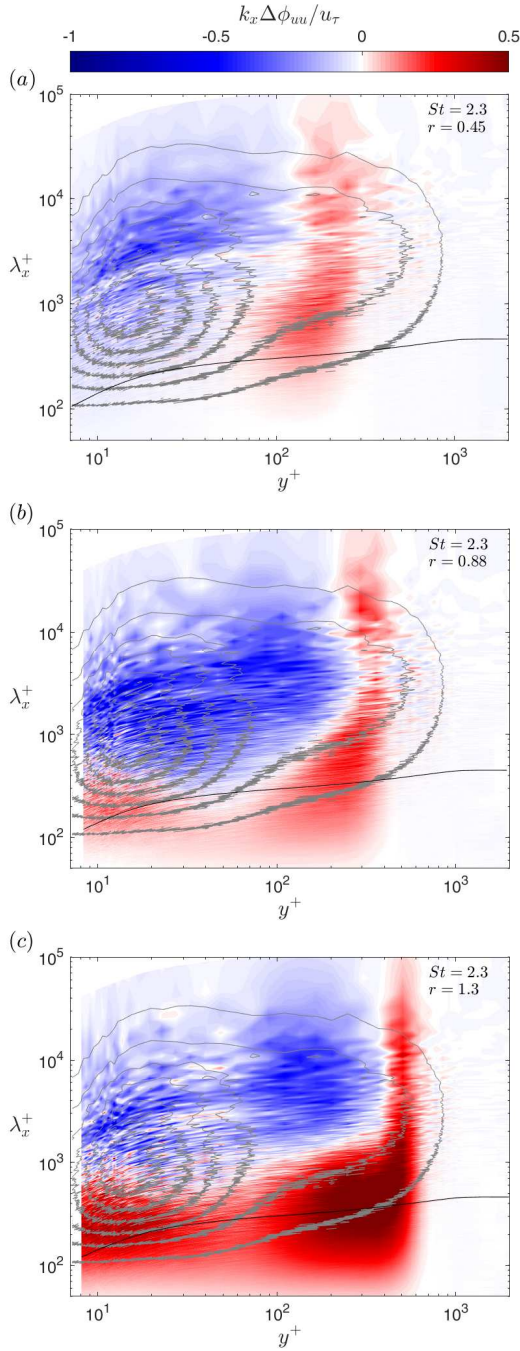


Figure 3. Difference in pre-multiplied power spectral density of u' ($k_x \Delta \phi_{u'u'} / u_\tau^2$) with and without synthetic jet forcing as a function of wall-normal distance for three blowing ratio cases, $r = 0.45, 0.88$ and 1.3 at $St = 2.3$. The grey contour levels are in increments of $k_x \phi_{u'u', \text{uncont}} / u_\tau^2 = 0.3$, and the solid line is the frequency of the jet.

r , there is an increase in u' near the synthetic jet frequency across the boundary layer, including the location of the near-wall cycle ($y^+ = 15$). This is not seen for the $r = 0.45$ case, as the only increase is seen close to the y location where the synthetic jet crosses the measurement plane.

Similarly, across St there is a decrease in the contribution to u' from the largest scales, as seen in Figures 3a and 4. For the $St = 0.045$ case, the wavelength implied by the frequency of the synthetic jets is very similar to the large scales and there is actually a very large increase in the contribution

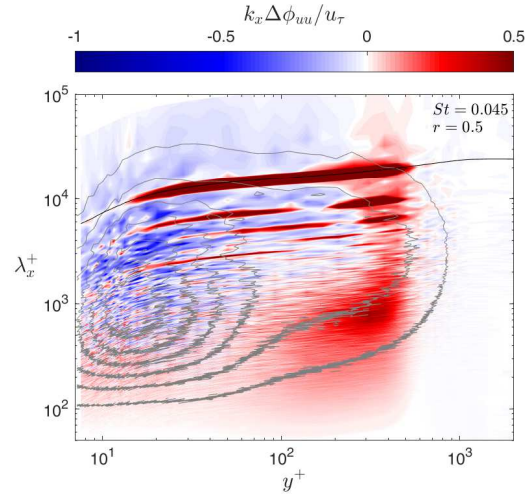


Figure 4. Difference in pre-multiplied power spectral density of u' ($k_x \Delta \phi_{u'u'} / u_\tau^2$) with and without synthetic jet forcing as a function of wall-normal distance at $St = 0.045$ and $r = 0.5$. The grey contour levels are in increments of $k_x \phi_{u'u', \text{uncont}} / u_\tau^2 = 0.3$, and the solid line is the frequency of the jet.

to u' at wavelengths close to this wavelength, and associated harmonics, from about the buffer layer up to the intersection point of the jet with our measurement plane. At this intersection point there is an increase in u' across all wavelengths, something present for all cases shown with different r . Interestingly, the largest increase in u' is at the smallest scales for the $St = 0.045$, similar to all cases at $St = 2.3$, indicating that it is not related to the frequency of the jets, which might be assumed by looking at Figure 3 alone. The increase in u' at the wavelength implied by the synthetic jet frequency for the $St = 0.045$ case in Figure 4 indicates that the frequency of the jet is low enough for a periodic vortical structure that is still coherent when it reaches $x = 2\delta$. Conversely, the lack of u' contribution at the synthetic jet frequency for the cases in Figure 3 indicates a jet that no longer has periodic structure, either because the individual vortices have broken down, or because they have merged to form a larger structure. Figures 3 and 4 appear very similar to that shown by Abbassi *et al.* (2017), which was for a pulsed jet issuing from a streamwise-oriented rectangular orifice targeting the upwash and downwash regions of large-scale streaks in the log-region. In particular, they also notice a decrease in the large wavelength contribution to u' . In addition, Chin *et al.* (2017) show a similar decrease in the large-scale contribution to u' from large eddy simulations of a turbulent boundary layer exposed to a large eddy breakup device. However, in their results, they also see a sizeable increase in u' fluctuations at a range of scales just smaller than those where they see a decrease, indicating a breakdown of large eddies into smaller eddies.

In addition to the premultiplied spectra of u' , in Figure 5 we show the premultiplied spectra of τ_w' for all cases shown in Figures 3 and 4 and with the spectrum of the unforced baseline case. We plot the spectra simply as a function of frequency to avoid selecting a potentially suspect convection velocity for τ_w to use with Taylor's hypothesis. We observe that for all forced cases, there is a decrease in the spectra at the lower frequencies, corresponding to large wavelength fluctuations. For all but the $St = 2.3, r = 0.88$

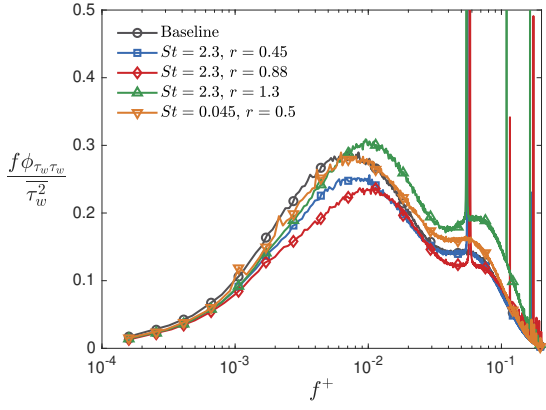


Figure 5. Pre-multiplied power spectral density of τ_w' for the forcing conditions listed in the legend.

case there is an increase in the spectra at higher frequencies, potentially indicating a transfer of energy from the larger to smaller scales with forcing. In general, the trend in Figure 5 matches the trend seen at the nearest wall-normal station of Figures 3 and 4. Comparing across r , we see that the spectra decrease with increasing r from $r = 0.45$ to $r = 0.88$ before decreasing from $r = 0.88$ to $r = 1.3$ for all frequencies. Comparing $St = 2.3$ with $St = 0.045$ at $r = 0.5$, we see that the spectrum is lower for all frequencies at $St = 2.3$. The large peaks present in the spectra are associated with the forcing frequency of the jet. The peaks are particularly large because both the actuator and shear stress sensor are mounted directly to the wall, meaning that vibrations induced by the actuator in the boundary layer plate are easily transferred to the sensor.

Simultaneous measurements of the streamwise velocity fluctuations in the boundary layer and the wall shear stress allow us to see how the impact of the jets on the boundary layer affects the correlation between the boundary layer and the wall. To show this, we compute the magnitude squared coherence:

$$\gamma_{u' \tau_w'}^2 = \frac{|\phi_{u' \tau_w'}|^2}{\phi_{u' u'} \phi_{\tau_w' \tau_w'}} \quad (7)$$

The difference with and without synthetic jet forcing is shown in Figure 6, as a function of hot-wire wall normal distance and for the three blowing ratios shown in Figure 3. Additionally, contours of the baseline magnitude squared coherence are indicated in grey. These figures show that there is a decrease in the correlation for each r . In Figure 6a, there is a decrease across all coherent scales at the top of the log-region. This is the location identified in Figure 3a where the jet crosses our measurement plane. An increased correlation is also observed closer to the wall and at smaller wavelengths (albeit still large wavelengths relative to the lowest wavelengths in the flow). As r is increased, there is an increased reduction of the correlation of the large-scales. For $r = 0.88$ in Figure 3b, this appears to still be confined to the smallest coherent scales, but for $r = 1.3$ in Figure 3c, the correlation has been substantially reduced for all scales and wall-normal locations in the log-region and above. There may be a continued decrease in the correlation closer to the wall, but we do not observe it here, as the heat transfer from the hot-wire to the wall may be masking it.

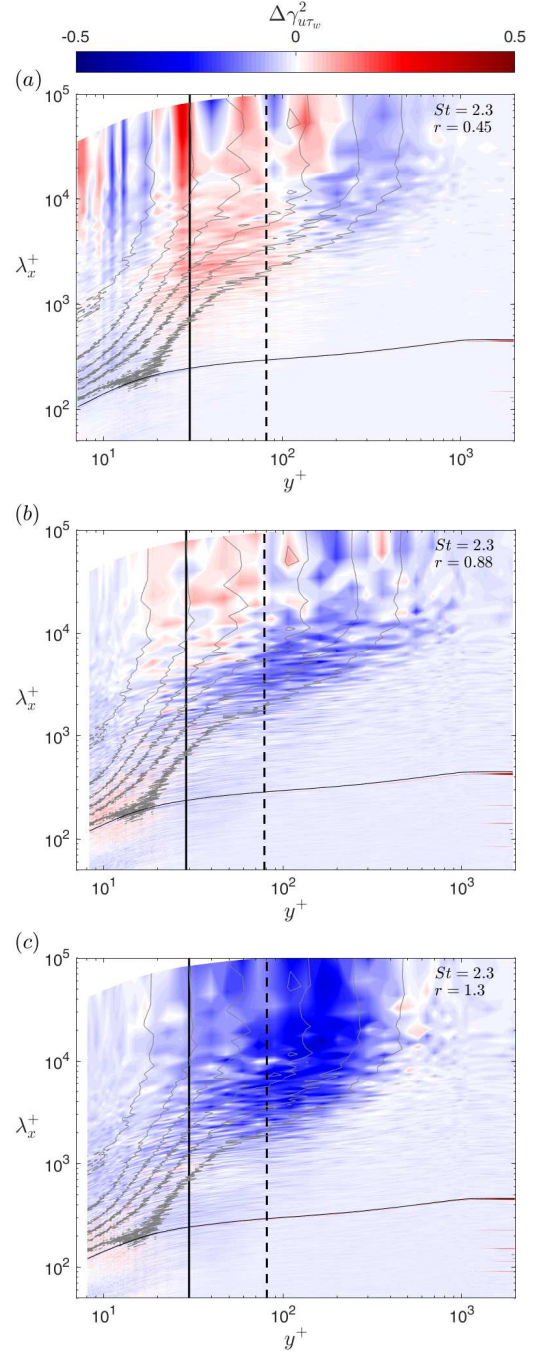


Figure 6. Difference in magnitude squared coherence of u' and τ_w' with and without synthetic jet forcing as a function of wall-normal distance for three blowing ratio cases, $r = 0.45, 0.88$ and 1.3 at $St = 2.3$. The grey contour levels are the uncontrolled magnitude squared coherence in increments of 0.14 , and the solid line is the frequency of the jet.

To compare across St , $\Delta\gamma^2$ is shown in Figure 7 for $St = 0.045$ and $r = 0.5$. The effect here is much stronger than was observed for $St = 2.3$ at a similar r in Figure 6a. Like Figure 6c at higher r , there is a decrease in the correlation for all scales that were originally correlated, and this extends throughout the log-region. Furthermore, the largest decrease in coherence is associated with the wavelengths near that implied by the synthetic jet frequency.

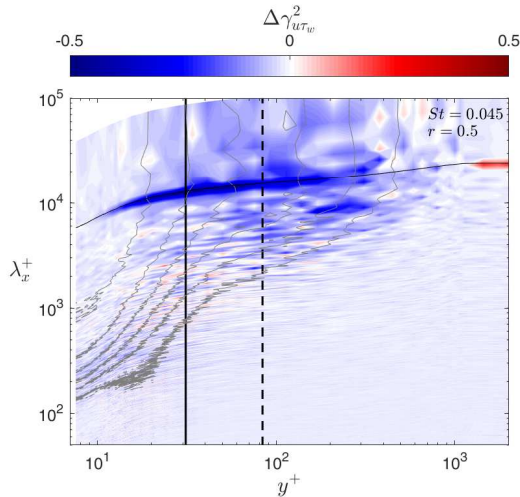


Figure 7. Difference in magnitude squared coherence of u' and τ_w^2 with and without synthetic jet forcing as a function of wall-normal distance at $St = 0.045$ and $r = 0.5$. The grey contour levels are the magnitude squared coherence in increments of 0.14, and the solid line is the frequency of the jet.

CONCLUSION

The preceding has shown that synthetic jets, irrespective of their frequency and amplitude (at least within the bounds of our measurements), cause a reduction in the strength of large wavelength fluctuations. This reduction of large-scale fluctuations agrees with previous work done by other researchers targeting the log-region of a turbulent boundary layer. In addition, we have also observed a reduction in correlation between the fluctuations in the boundary layer and those at the wall for large wavelengths. This indicates that synthetic jets are able to weaken large-scale structures that extend down to the wall or at least the effect that they have on the wall. This is important because it has been shown previously that the larger scales are more dominant at the higher Re_τ corresponding to most applications of engineering interest. Furthermore, the modulating effect of the large scales on the small scales suggests that the large scales in the log layer affect the small scales in the inner layer and hence the near-wall cycle.

These results show that it is possible to interact with and weaken the large scales in the flow with synthetic jets, but it is not yet clear exactly how this effect is manifested and how the modulation of the small scales is impacted. Future work will look into the mechanism(s) whereby the large-scale correlation of the boundary layer with the wall is weakened under synthetic jet forcing. We will investigate synthetic jets with varied vortical structures issuing into a turbulent boundary layer to understand their distinct effects.

ACKNOWLEDGEMENTS

The authors acknowledge the financial support of NSERC, and thank Dr. Mark Sheplak and IC² for making the shear stress sensor available for this work.

REFERENCES

Abbassi, M. R., Baars, W. J., Hutchins, N. & Marusic, I. 2017 Skin-friction drag reduction in a high-Reynolds-

number turbulent boundary layer via real-time control of large-scale structures. *International Journal of Heat and Fluid Flow* **67**, 30–41.

del Álamo, J. C. & Jiménez, J. 2003 Spectra of the very large anisotropic scales in turbulent channels. *Physics of Fluids* **15**, L41–44.

Chin, C., Örlü, R., Monty, J., Hutchins, N., Ooi, A. & Schlatter, P. 2017 Simulation of a large-eddy-break-up device (LEBU) in a moderate Reynolds number turbulent boundary layer. *Flow, Turbulence and Combustion* **98**, 445–460.

Ganapathisubramani, B., Hutchins, N., Hambleton, W. T., Longmire, E. K. & Marusic, I. 2005 Investigation of large-scale coherence in a turbulent boundary layer using two-point correlations. *Journal of Fluid Mechanics* **524**, 57–80.

Ganapathisubramani, B., Hutchins, N., Monty, J. P., Chung, D. & Marusic, I. 2012 Amplitude and frequency modulation in wall turbulence. *Journal of Fluid Mechanics* **712**, 61–91.

Hanson, R. E., Buckley, H. P. & Lavoie, P. 2012 Aerodynamic optimization of the flat-plate leading edge for experimental studies of laminar and transitional boundary layers. *Experiments in Fluids* **53**, 863–871.

Hoyas, S. & Jiménez, J. 2006 Scaling of the velocity fluctuations in turbulent channels up to $Re_\tau = 2003$. *Physics of Fluids* **18**, 011702.

Hutchins, N. & Marusic, I. 2007a Evidence of very long meandering features in the logarithmic region of turbulent boundary layers. *Journal of Fluid Mechanics* **579**, 1–28.

Hutchins, N. & Marusic, I. 2007b Large-scale influences in near-wall turbulence. *Philosophical Transactions of the Royal Society A* **365**, 647–664.

Jabbal, M. & Zhong, S. 2008 The near wall effect of synthetic jets in a boundary layer. *International Journal of Heat and Fluid Flow* **29**, 119–130.

Jiménez, J. & Pinelli, A. 1999 The autonomous cycle of near-wall turbulence. *Journal of Fluid Mechanics* **389**, 335–359.

Marusic, M., Mathis, R. & Hutchins, N. 2010 High Reynolds number effects in wall turbulence. *International Journal of Heat and Fluid Flow* **31**, 011702.

Mathis, R., Hutchins, N. & Marusic, I. 2009 Large-scale amplitude modulation of the small-scale structures in turbulent boundary layers. *Journal of Fluid Mechanics* **628**, 311–337.

Mills, D. A., Patterson, W. C., Keane, C. & Sheplak, M. 2018 Characterization of a fully-differential capacitive wall shear stress sensor for low-speed wind tunnels. In *2018 AIAA Aerospace Sciences Meeting*, p. 0301. Kissimmee, FL.

Sau, R. & Mahesh, K. 2008 Dynamics and mixing of vortex rings in crossflow. *Journal of Fluid Mechanics* **604**, 389–409.

Schoppa, W. & Hussain, F. 2002 Coherent structure generation in near-wall turbulence. *Journal of Fluid Mechanics* **453**, 57–108.

Van Buren, T., Whalen, E. & Amitay, M. 2014 Vortex formation of a finite-span synthetic jet: effect of rectangular orifice geometry. *Journal of Fluid Mechanics* **745**, 180–207.

Waleffe, F. 1997 On a self-sustaining process in shear flows. *Physics of Fluids* **9**, 883–900.